Electronic Supplementary Material (ESI) for RSC Advances.

Construction of new ternary α-MoO_3-WO_3/CdS solar nanophotocatalyst towards clean water and hydrogen production from artificial wastewater using optimal design methodology

Heba H. El-Maghrabi [1]; Hager R. Ali [2,3]; Sherif A. Younis [2,3*]

[1] Catalysis Division, Petroleum Refining Department, Egyptian Petroleum Research Institute, 11727 Nasr City, Cairo, Egypt.

[2] Spectroscopic Division, Analysis and Evaluation Department, Egyptian Petroleum Research Institute, 11727 Nasr City, Cairo, Egypt.

[3]Liquid chromatography Unit, Central laboratories, Egyptian Petroleum research Institute, 11727 Nasr City, Cairo, Egypt.

***Correspondence:** Sherif A. Younis

E-mail: sherifali_r@yahoo.com; sherifali@epri.sci.eg

Tel.: (+201) 228877458; **Fax:** (+202) 22747433

2. Experimental Section

2.1.Materials

All of the reagents were used as received without any further purification. Deionized water was used throughout the experiments. Ethylenediamine, Cd $(NO_3)_2.$ $4H_2O$ and NH_2CSNH_2 were purchased from Fluka. Ammonium tungstate (99.99 %,), ammonium molybdate (99.99 %), ethylene glycol (99.5%) and citric acid (99.5%) were purchased from Merck.

2.2. Synthesis of CdS, WO_3 and α-MoO_3 nanomaterials

For preparation of CdS nanowire, a mixed solution of $Cd(NO_3)_24H_2O$ and NH_2CSNH_2 was added into a Teflon-lined stainless steel autoclave filled with ethylenediamine to 80% of its capacity. The autoclave was maintained at 160 ^oC for 48 h for solvothermal reaction and then allowed to cool to room temperature. The colored precipitate was filtered and washed with absolute ethanol and deionized water [1,2], then vacuum dried overnight.

Both WO_3 and α-MoO_3 nanoparticles were prepared by the modified Pechini method [3,4]. In a typical procedure, ammonium salt (ammonium tungstate or ammonium molybdate) was dissolved in hot deionized water till clear solution obtained. Then, known amount of citric acid and ethylene glycol were added simultaneously under continuous stirring for 2 h followed by microwave heating to form the polymeric resin. The dark blue transparent glassy resin obtained was ground into a powder, then subjected to the calcination process at 500°C for 4 h then storage in caped glass bottles until used. The preparation of binary and ternary nanocomposites samples was carried out using simplex centroid design (SCD) matrix listed in in Table (S1) and Fig. (S1a).

2.3. Characterizations

The phase structure of the catalysts was determined by Powder X-ray diffractometry "PXRD" (Xpert PRO, PAN analytical, Netherlands) at Cu Kα radiation (λ=0.15417) in the step of 0.1° (2 Θ). For phase identification purposes, automatic JCPDS library search and match were used. The Raman spectrum was obtained at a laser wavelength of 532 nm and room temperature in the spectral range of 1500–100 cm^{-1} using Sentra instrument (Bruker, Germany) on a microscope slide with X 80 lens. The Fourier transform infrared spectroscopy (FTIR) measurement was recorded on a spectrum one spectrometer (Perkin Elmer, USA) in the range of 4000–400 cm^{-1} using the KBr disc as the reference. Morphological study was

performed with a JEOL JEM-2100 high-resolution transmission electron microscope (HRTEM) at 200 kV equipped with EDS (D2-LN2 free silicon drift detector – Oxford X-Max). The surface area was determined from the adsorption of nitrogen gas at liquid nitrogen temperature (–195.8 ºC) using NONA3200e (Quantachrome – USA). Prior to surface area measurements, all samples were perfectly degassed at 573 K and 10^{-4} Torr overnight. The optical properties were carried out by UV-Vis diffuse reflectance and photoluminescence (PL) (Jasco model V-570) spectrophotometer at room temperature to estimate the energy band gap.

2.4. Photocatalytic studies

The photocatalytic experiments were operated in a 200 ml closed cylindrical quartz reactor had connectors for the gas outlet and solution sampling.

First, for ODOE design (Table S1-S2 and Fig. S1-S2), a tap water (TDS 420 mg/l) contaminated with a definite concentration of benzoic acid was used as a synthetic wastewater to evaluate the photocatalytic activities of the prepared single, binary, and ternary phoyocatalysts. The photodegradation experiments were carried out as follows; the definite amount of catalyst dose was suspended in a 100 ml synthetic wastewater containing known concentrations of benzoic acid at the desired pH (adjusted with 0.1 mol HCL or NaOH). Then the reaction sample was vigorously stirred in the dark for 1h to enable an adsorption–desorption equilibrium before illumination. After that, the whole sample was transferred to the photocatalytic reactor and exposed to ultraviolet (20 W, 365 nm) and visible (Linear halogen lamp 500 W, and > 400 nm) irradiations with continuous stirring at 150 rpm for 4 h. At the end of the photoreaction time, the treated artificial wastewater samples were collected from the photoreactor and centrifuged at 6,000 x g for 10 minutes. The benzoic acid photodegradation rate in the clean supernatant solution was monitored and determined by high-performance liquid chromatograph (HPLC model Agilent 1200 series). In our case, the best optimization procedure using ODOE approach is to consider the economics and efficiencies of the treatment by the developed photocatalyst along with maximizing response results.

Second, from a selected Egyptian industrial plant, a real wastewater effluent was collected to investigate the capability of the α-$MoO_{3\ (0.03)}$–$WO_{3\ (0.36)}$/$CdS_{\ (0.61)}$ photocatalyst for solar energy utilization to remediate industrial wastewaters and generate hydrogen simultaneously. The characteristics of the collected wastewater were TDS، 780 mg/L, total organic carbons (TOC), 246.75 mg/L and pH, 5.49. The sunny day between 10.00 am and 4.00 pm during March and April-2016 was used as the solar-light source. The total

photocatalytic reaction time was 6 h. Photo-irradiation was operated under visible and direct solar lights. After given time intervals, the photocatalytic response of the ternary photocatalyst was evaluated in terms of the TOC removal with CO_2, and H_2 production rates.

2.5. Analytical Procedures

The benzoic acid photodegradation rate was monitored by high-performance liquid chromatograph (HPLC model Agilent 1200 series) equipped with photodiode array detector (set at 220 nm) and a reverse-phase C-18 column (15 cm × 4.6 mm I.D., 5 μm) operated under temperature controller set at 308 K. The mobile phase consists of 70% buffer water with acetic acid (pH~ 4.2) and 30% Acetonitrile operated in isocratic mode with flow rate of 1 ml/min. The gas generated during photoctalytic processes was collected in gas trap system degassed previously by passing an inert N_2 gas. The collected gas content was determined and quantified using a gas chromatography (GC Perkin Elmer model Clarus 500) instrument. The GC equipped with a packed chromatograph 102 stainless steel column and a thermal conductivity (TCD) detector and N_2 as a carrier gas with 12 ml/min flow rate. The amount of TOC concentrations in the wastewater samples before and after treatment processes were monitored by TOC (Shimadzu 5000A) analyzer. The total dissolved solids (TDS) of the collected wastewater sample was determined according to ASTM D 5907.

Table S1: SCD matrix of the prepared nanocomposites samples and their photodegradation responses (%) under ultraviolet and visible irradiations.

Run	Catalysts combinatorial ratios			Light factors	Photodegradation (%)		Residual	Error%
	A	B	C		Actual	Predicted		
1	0.67	0.17	0.17	Vis	43.20	44.01	-0.81	-1.87
2	0.17	0.67	0.17	UV	46.82	47.35	-0.53	-1.13
3	1.00	0.00	0.00	Vis	38.47	38.52	-0.05	-0.13
4	0.33	0.33	0.33	UV	44.99	45.49	-0.50	-1.11
5	0.17	0.67	0.17	Vis	33.24	35.15	-1.91	-5.75
6	0.00	0.50	0.50	UV	8.70	7.46	1.24	14.25
7	0.00	1.00	0.00	Vis	26.00	25.68	0.32	1.23
8	0.17	0.17	0.67	Vis	14.96	14.67	0.29	1.94
9	0.00	0.00	1.00	Vis	3.36	3.77	-0.41	-12.20
10	0.17	0.17	0.67	UV	19.20	20.98	-1.78	-9.27
11	1.00	0.00	0.00	UV	44.19	44.53	-0.34	-0.77
12	0.00	1.00	0.00	UV	45.35	45.48	-0.13	-0.29
13	0.33	0.33	0.33	Vis	31.81	32.19	-0.38	-1.19
14	0.50	0.00	0.50	Vis	20.24	19.63	0.61	3.01
15	0.00	0.00	1.00	UV	7.45	7.16	0.29	3.89
16	0.67	0.17	0.17	UV	57.04	56.91	0.13	0.23
17	0.50	0.50	0.00	Vis	69.50	68.15	1.35	1.94
18	0.50	0.00	0.50	UV	38.11	37.10	1.01	2.65
19	0.00	0.50	0.50	Vis	6.84	5.86	0.98	14.33
20	0.50	0.50	0.00	UV	78.49	77.89	0.60	0.76

Table S2: Three-levels BBD variable levels for benzoic acid photodegradation under visible-activation

Code	Independent variables	Actual levels		
		Low (-1)	Medium (0)	High (+1)
X_1	catalyst dose (g/l)	0.5	1.0	1.5
X_2	Initial benzoic acid concentration (mg/l)	50	100	150
X_3	Reaction pH	4	7	10

Herein, 17 BBD runs were developed based on the combination of two factors variables designs through all matrix design and the third factor is preserved at central value. The BBD variables' levels were consecutively coded as (−1), (0) and (1) for low, central, and high levels (Table S2) using the following dimensionless equations:

$$\text{Dese} = \frac{X_1 - 1}{0.5} \quad \text{(Eq. S1)}$$

$$\text{Concentrations} = \frac{X_2 - 100}{50} \quad \text{(Eq. S2)}$$

$$\text{pH} = \frac{X_3 - 7}{4} \quad \text{(Eq. S3)}$$

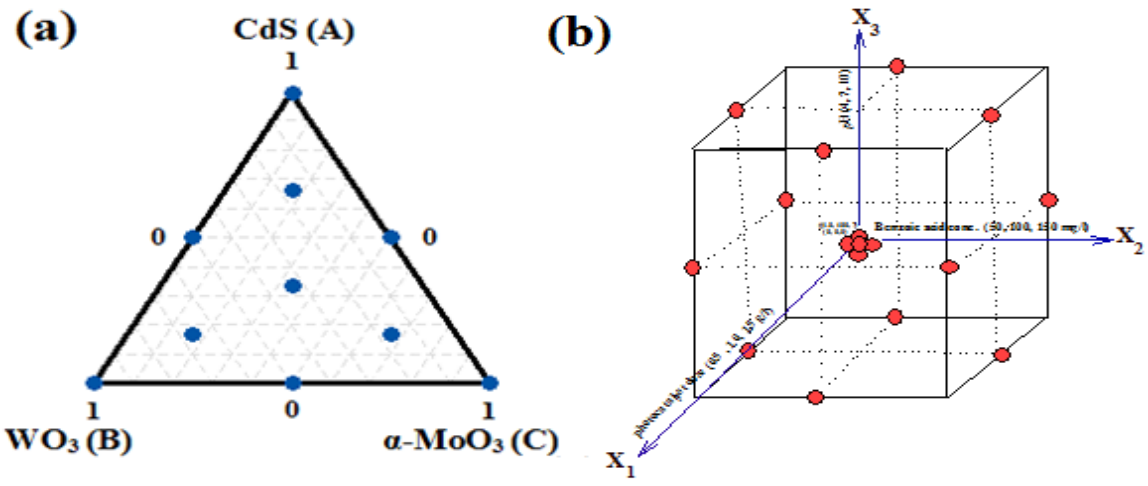

Fig. S1: (a) 10 Points SCD and (b) the geometry of 17 points BBD as a function of three independent variables on benzoic acid photodegradation rate under ultraviolet and visible lights.

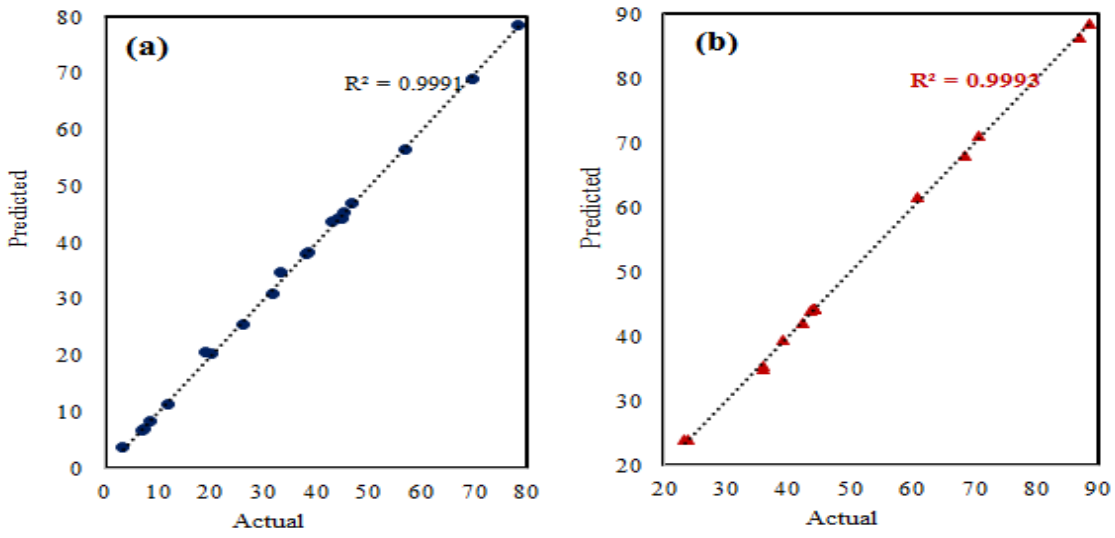

Fig. S2: Plot of the actual versus predicted response values for benzoic acid photodegradation using (a) SCD and (b) BBD approaches.

3. Results and discussion

3.1. Development of α-$MoO_{3(0.03)}$-$WO_{3(0.36)}$/$CdS_{(0.61)}$ nanocomposite using ODOE approach

From Table (S1), the light factor shows a high significant influence on the photodegradation rate using the prepared single photocatalysts (F-test 60.16 and p<0.0001) compared to binary and ternary photocatalysts (F-test 29.12 and p=0.001) (Table 1). Among nanocomposite photocatalysts, the photocatalytic activities of binary WO_3/CdS, and ternary α-MoO_3-WO_3/CdS show an independence on light types (p > 0.05, Table 1). The contour plots (Fig. 1a) show that the total effect of the composite mixtures and the steepness of its response trace relative to its centroid reference blend. The cox trace plot (Fig. 1b) confirms that the photodegradation results are mainly dependent on the catalyst combinations ratios, and the CdS (A) and α-MoO_3 (C) have the highest influential effect on the response rates with unparalleled directions.

3.2. Characterization

3.2.1. Mineralogical and morphological analysis

The PXRD patterns of the prepared samples are shown in Fig. (2a). For CdS, the PXRD shows sharp and narrow diffraction at $2\theta \approx 24.99°$ (100), 26.91° (002), 28.41° (101), 43.64° (110), 47.8° (103), and 51.9° (112), suggesting a high purity and complete formation of CdS nanowires. The WO_3 PXRD pattern between 22° ~ 25° have three well-defined peaks at 2θ = 23.13°, 24.13° and 24.48°, corresponding to Miller indices (002), (020) and (200) diffractions of monoclinic crystal structure, which is the most WO_3 stable phase at room temperature. Furthermore, the PXRD diffraction of α-MoO_3 can be indexed to a high crystallinity orthorhombic phase at 2θ of 12.8° (020) instead of monoclinic with a preferred orientation. According to the JCPDS database, the calculating lattice parameters (Å) using the plane spacing equation for CdS nanowires were a = 4.12 Å and c = 6.724 Å and orthorhombic α-MoO_3 lattice parameters (Å) were a = 3.96, b = 13.86, and c = 3.70 Å. Whereas, the PXRD of WO_3 corresponding to monoclinic crystal structure with d spacing 0.385, 0.377 and 0.365 nm and interlayer spacing 0.77, 0.76 and 0.73 nm, respectively.

Fig. (S3) shows the FTIR spectra of the prepared photocatalyst. The FTIR broadband at about 3420 cm^{-1} in all the spectrum corresponds to the stretching and bending vibration mode of the physically adsorbed H_2O. For the single CdS catalyst, the absorption band located at 1113 cm^{-1} is assigned to the Cd–S vibration mode. For WO_3, the FTIR bands

observed at 748 cm^{-1} (W–O bending modes) and 807 cm^{-1} (W–O stretching modes) identifying the crystalline WO_3. The three strong vibrations bands detected in α-MoO_3 at 621, 874 and 993 cm^{-1} were associated with the stretching mode of oxygen linked with three metal atoms, the stretching mode of oxygen in the Mo–O–Mo units, and the Mo=O stretching mode of a layered orthorhombic α-MoO_3 phase, respectively. The weak vibrations detected at 1384 cm^{-1} was also associated with the vibration mode of the Mo–OH bond. Overall, the FTIR peaks of α-$MoO_{3\ (0.03)}$–$WO_{3\ (0.36)}$ / $CdS_{(0.61)}$ ternary photocatalyst showed all the vibration modes assigned to α-MoO_3, WO_3 and CdS catalysts (Fig. S3).

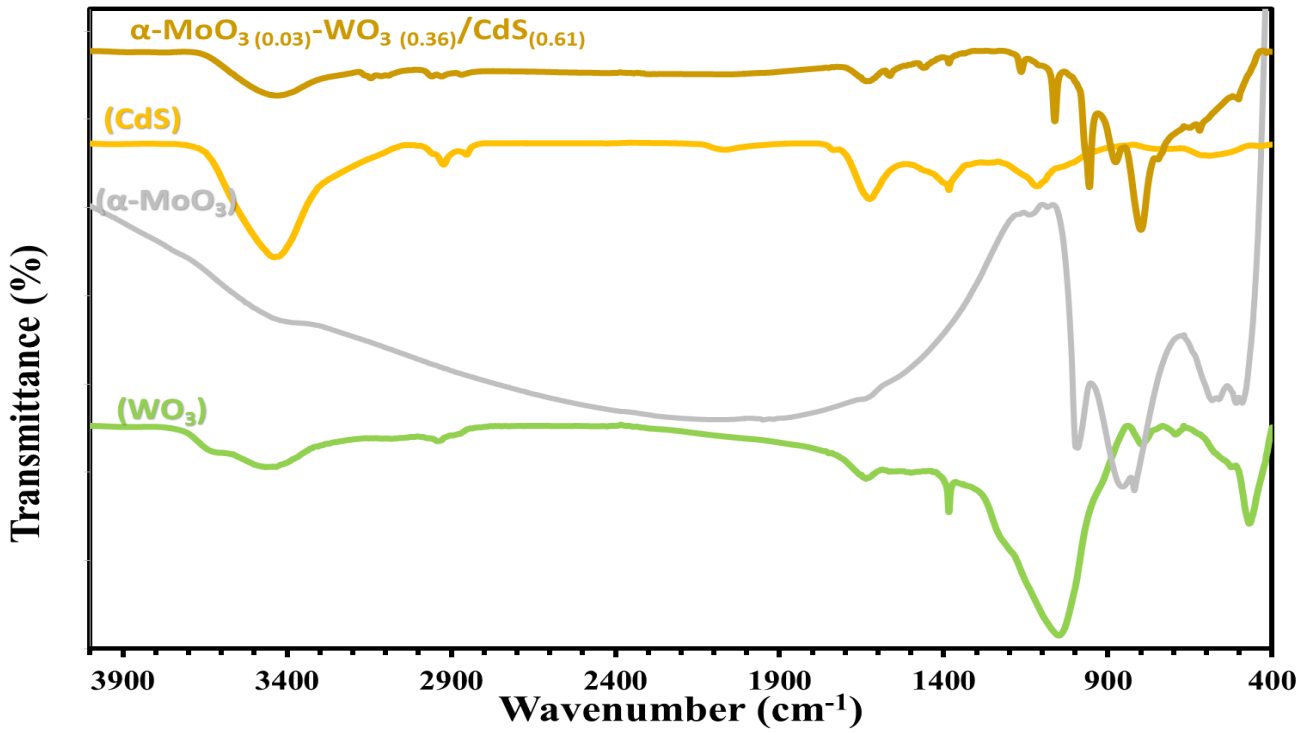

Fig. S3: The FTIR spectra of the prepared nanostructure photocatalysts.

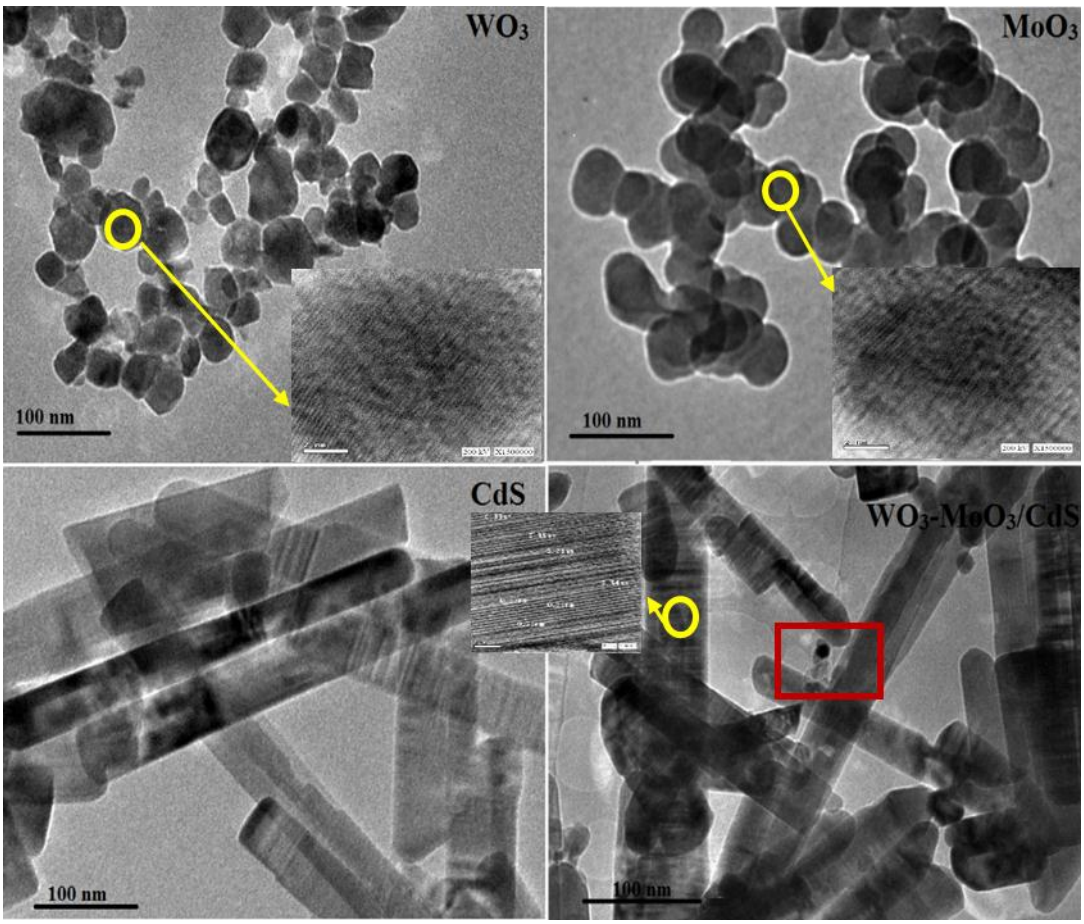

Fig. (S4): HRTEM images and lattices of the prepared catalysts (O symbol is the HRTEM lattice area; and ▭ symbol is the area selected for the EDS spectrum, and SAED pattern of nanocomposite (Fig. 3))

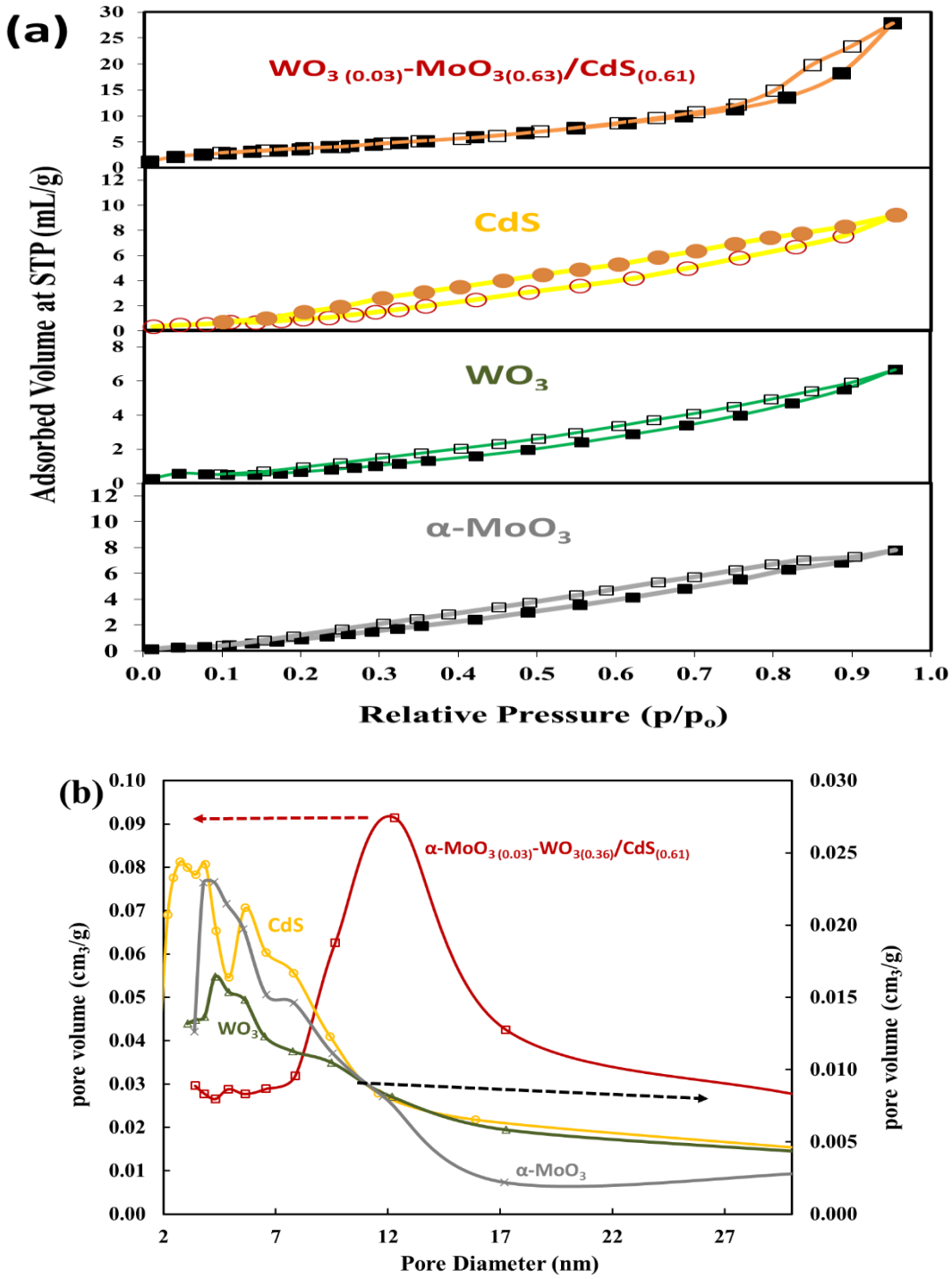

Fig. S5: (a) The N_2 adsorption/desorption isotherms and (b) pore volume distribution of the prepared photocatalysts.

Table S3: The detailed data of the variations in BET surface area, pore volume and average pore diameter of prepared catalysts.

Samples	BET surface area (m^2/g)	Pore volume (cm^3/g)	Average pore diameter (nm)[a]
MoO_3	**8.011**	**0.012**	**3.3738**
WO_3	**6.582**	**0.011**	**3.0656**
CdS	**17.736**	**0.019**	**2.4478**
α-$MoO_{3\ 0.03}$-$WO_{3\ 0.36}$/$CdS_{0.61}$	**18.145**	**0.044**	**3.411**

[a] Determined by the Barrett–Joyner–Halenda (BJH) method.

3.2.2. Optical analysis

The synergetic effect of the α-$MoO_{3\ (0.03)}$–$WO_{3\ (0.36)}$/$CdS_{\ (0.61)}$ ternary heterojunction photocatalyst on the light absorption was studied to determine the performance of photocatalytic properties. From the UV-vis DRS (Fig. 4a), the optical band gap of the prepared samples can be determined from the sharply falling transmission region in the wavelength range 350-550 nm. According to Tauc's law, the absorption coefficient has the following energy dependence ($\alpha h\nu = B(h\nu - E_g)^n$). Where α is the absorption coefficient, $h\nu$ is the incident photon energy, B is a constant, and n is either 2 or ½ for direct and indirect transitions, respectively. It is known that α-MoO_3, WO_3, and CdS crystals are an indirect-gap semiconductor, thus, *n* value of 2 is assumed here. So the straight line plots between $(\alpha h\nu)^{0.5}$ versus photon energy ($h\nu$), which is extended on the x-axis ($h\nu$) to provide the value of the optical band gap (E_g) [5,6]. The data obtained illustrates that the spectrum of pure α-MoO_3 is a pale gray colored powder having an absorption cutoff edge at 380 nm, corresponding to a band gap of 3.05 eV. The light green color of WO_3 sample gives an absorption edge at 460 nm with a band gap of 2.72 eV. The pale yellow colored CdS nanorods powder exhibits a band edge at 480 nm with the band gap of 2.42 eV. More importantly, the band edge for α-$MoO_{3\ (0.03)}$–$WO_{3\ (0.36)}$/$CdS_{\ (0.61)}$ ternary nanocomposite is observed at 508 nm with the lowest band gap of 2.33 eV, suggesting the ability of the developed nanocomposite to harvest broad wavelengths. Moreover, the PL emission spectra is frequently performed to study the transfer and recombination of photo-generated electrons-hole pairs in photocatalysts [7] as presented in main text.

3.3. Photocatalytic activities of α-$MoO_{3(0.03)}$–$WO_{3\ (0.36)}$ /$CdS_{(0.61)}$) ternary photocatalyst

3.3.1. BBD regression modeling

Table S4: Model statistics for benzoic acid photodegradation by α-$MoO_{3\ (0.03)}$-$WO_{3\ (0.36)}$ /$CdS_{(0.61)}$ photocatalyst under visible light.

Model	Std. Dev.	R^2	Adj R^2	Pred R^2	PRESS	RSEP	Remark
Linear	5.90	0.923	0.905	0.862	815.59	9.77	Not suggested
2FI	5.31	0.952	0.923	0.848	897.19	7.71	Not suggested
Quadratic	0.71	0.998	0.997	0.991	55.83	0.87	Suggested
Cubic	0.14	1.000	1.000	--	--	0.13	Aliased

From Table (S4) above, the very low PRESS (55.83) and RSEP (0.87%) statistic values for the quadratic model indicate the best structure in the numerical equation-fitting to the experimental data with the lowest error in the conducted design. This evident from the very high coefficients (pred R^2 0.991≈ adj$R^2$0.997) and F-test (F_{model} =1284.25 > critical $F_{0.05,9,7}$ = 3.68) with low probability (p-value) <0.0001 (Table 3). In addition, the quadratic model shows a high adequate precision ratio of 117.82, and a low coefficient of variation (C.V. =1.44%) and standard deviation of 0.71 compared to other investigated models. Therefore, it can infer that, at 95% confidence, the simulated equation (Eq. 9) is a statistically reliable to represent the relationship between the three studied variables levels and the benzoic acid photodegradation response using α-$MoO_{3\ (0.03)}$–$WO_{3\ (0.36)}$ / $CdS_{(0.61)}$ photocatalyst under visible light.

3.3.2. Estimation of interactive effect of experimental variables

Obviously, From ANOVA data (Table 3), the X_2X_3 interaction term and quadratic term of X_1^2 demonstrated the lowest effect on the benzoic acid photocatalytic rates (t= 1.83 and 2.96, F=3.59 and 5.81, p= 0.1 and 0.0467, respectively). In addition, from the static diagrams in Fig. (S6), it is remarkable the benzoic photdegradation response is proportionally affected by the hybrid photocatalyst dose (X_1); whilst, it is inversely affected by initial pollutants concentration (X_2) and pH (X_3). This may be due to dissociation of benzoic acid (pKa 4.2) to its benzoate (COO^-) in aqueous solution that is electrostatically attracted to the positively charged catalyst surface at lower pH. The Pareto chart in Fig. (S6a) shows that the lower X_2X_3 and X_1^2 coefficients values compared to other model components in Eq. (8), reflecting the least effect in prediction of the photodegradation rate using α-$MoO_{3\ (0.03)}$–WO_3

$_{(0.36)}$ / $CdS_{(0.61)}$ photocatalyst. Also, the negative coefficients sign for the four terms ofX_2,X_3, X_1X_2, and X_1X_3 represent an antagonistic or unfavorable effect on the photocatalytic response. However, a positive coefficients ofX_1, X_2^2 andX_3^2 indicate a synergistic and a favorable effect on photodegradation efficiency. Based on the obtained sum of square (SS) values (Table 3), the percentage of contribution (PC%) for the numerical components in Eq. (8) were calculated and schematically drawn in Fig. S (6b). Obviously, quadratic variables have a low significant effect on photo-response compared to that of the first order terms. As seen, the reaction pH showed the highest significant level with a contribution of 70.49%, and linear components reflected the highest significant level with a total linear contribution of 92.31% as compared to the interaction and quadratic terms with a total polynomial contribution of 2.91% and 4.73%, respectively.

Overall, based on the simultaneous cube plot response in Fig (5c), the maximum photodegradation response of 89.81% was seen at levels of (+1, -1, -1), while the minimum performances were shown at design space of (+1, +1, +1) and (-1, +1, +1) with percentage photodegradation of 25.09% and 24.45%, respectively at the constraints levels.

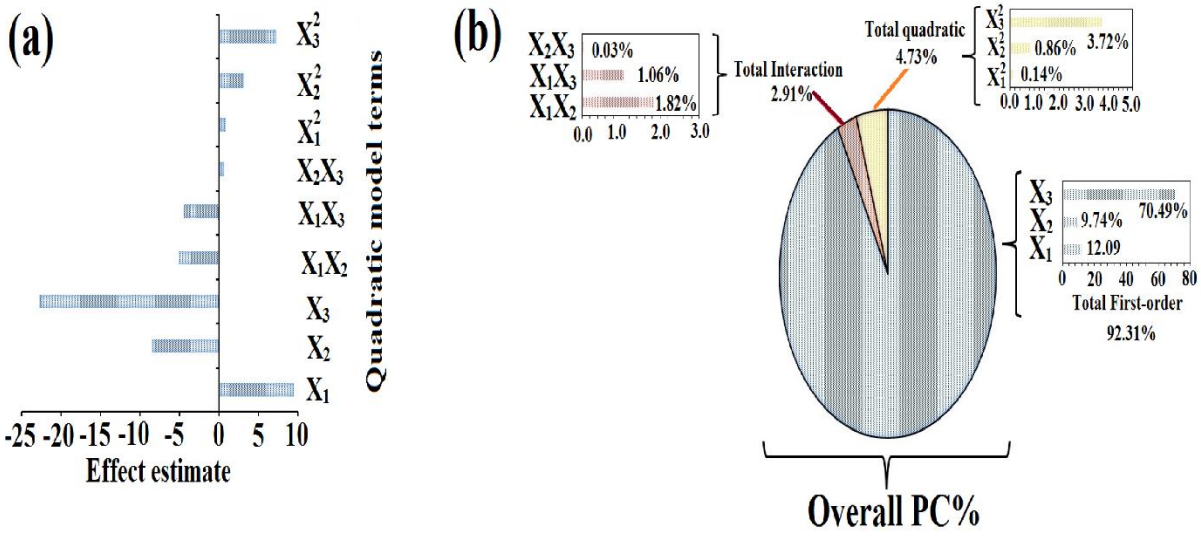

Fig. S6: (a) Pareto chart and (b) A detailed schematic contributions (PC%) showing the effect of the linear, interaction and quadratic model components on the photocatalytic efficiency.

3.4.Photocatalytic activity and hydrogen generation using α-$MoO_{3\ (0.03)}$–$WO_{3\ (0.36)}$/$CdS_{(0.61)}$

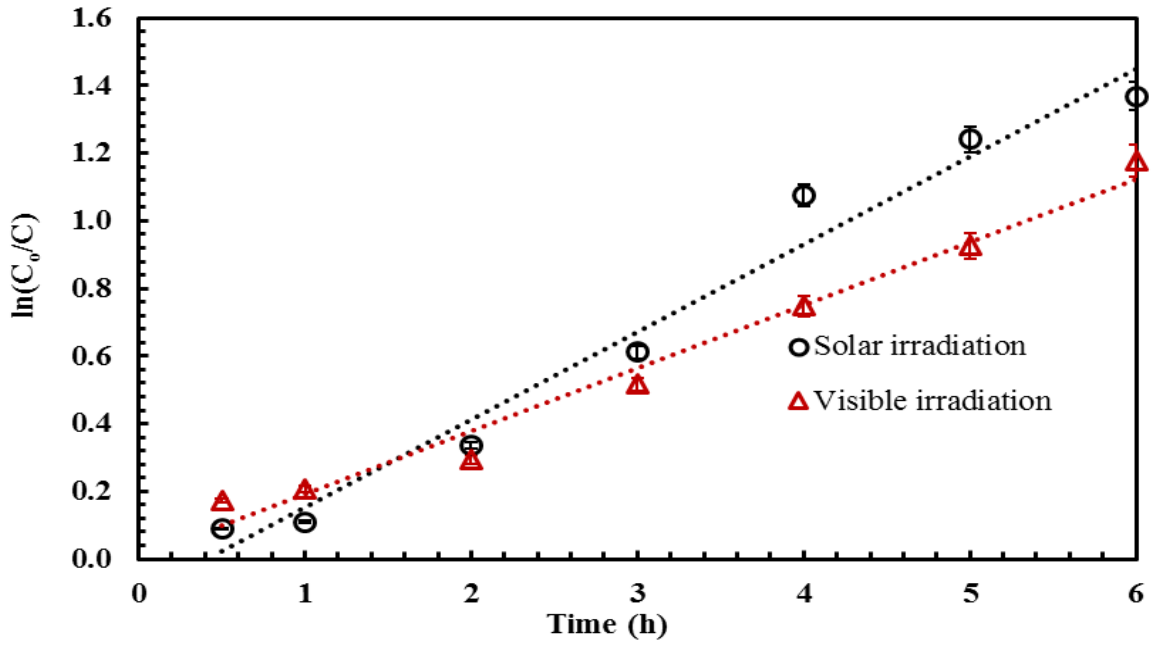

Fig. S7: apparent first-order kinetic of wastewater TOC under visible and solar irradiation.

In this case, an excellent linear correlation (R^2 = 0.974–0.982) of apparent first-order kinetic model was determined for the removal of TOC by α-$MoO_{3\ (0.03)}$–$WO_{3\ (0.36)}$ / $CdS_{(0.61)}$ ternary photocatalyst (Fig. S7). The calculated apparent first-order kinetic rate constants were 0.1867 h^{-1} and 0.2596 h^{-1} under visible and solar lights, respectively. The notable high photocatalytic reactions of α-$MoO_{3\ (0.03)}$–$WO_{3\ (0.36)}$ / $CdS_{\ (0.61)}$ under solar illumination may be attributed to the strong synergic effect and appropriate semiconductors composition in the ternary heterojunction system developed.

4. References

1 J. Yang, J.-H. Zeng, S.-H. Yu, L. Yang, G. Zhou and Y.-T. Qian, *Chem. Mater.*, 2000, **12**, 3259–3263.

2 Y. Li, X. Li, C. Yang and Y. Li, *J. Mater. Chem.*, 2003, **13**, 2641–2648.

3 H. Hassan, T. Zaki, S. Mikhail, A. Kandil and A. Farag, *ISRN Nanomater.*, 2012, **2012**.

4 T. Zaki, K. I. Kabel and H. Hassan, *Ceram. Int.*, 2012, **38**, 4861–4866.

5 H.-T. Sun, C. Cantalini, L. Lozzi, M. Passacantando, S. Santucci and M. Pelino, *Thin Solid Films*, 1996, **287**, 258–265.

6 F. S. Manciu, J. L. Enriquez, W. G. Durrer, Y. Yun, C. V Ramana and S. K. Gullapalli, *J. Mater. Res.*, 2010, **25**, 2401–2406.

7 J. Luo, X. Zhou, L. Ma and X. Xu, *J. Mol. Catal. A Chem.*, 2015, **410**, 168–176.